

Article

An Algorithm for Calculating the Parameter Selection Area of a Doubly-Fed Induction Generator Based on the Guardian Map Method

Yibo Wang, Futao Chen, Wei Jia and Rui Wang *

College of Information Science and Engineering, Northeastern University, Shenyang 110000, China; 2271028@stu.neu.edu.cn (Y.W.); 20224741@stu.neu.edu.cn (F.C.); 20214639@stu.neu.edu.cn (W.J.)

* Correspondence: wangrui@ise.neu.edu.cn

Abstract: Large-scale wind farms incorporating doubly-fed induction generators (DFIGs) are considered a promising direction for modern energy supply systems due to their role in reducing dependence on fossil energy sources. However, the dynamic interactions between DFIGs and AC grids sometimes lead to sub-synchronous oscillation (SSO) that threatens the safe and stable operation of wind power systems. Therefore, it is essential to develop a mathematical model and design an algorithm to quantitatively design the control parameters. Such algorithms are helpful in preventing or mitigating system stability problems coming from wind power connected to the grid and reducing damage to power equipment. The traditional state-space model is mainly established to determine the stable operating point and analyze the influence of parameters on the system operating mode. However, this method does not provide the selection area for the system parameters. To address this shortcoming, this paper introduces a modular state-space model for DFIGs containing series compensation lines and proposes an algorithm for calculating the parameter selection area based on the Guardian map method. First, a detailed modular state-space model based on the virtual synchronous generator (VSG) control is established. The modular model helps to reflect the relationship between state variables and focuses on describing the operating state of DFIGs in wind farms. Second, this paper focuses on the influence of VSG control parameters and compensation capacitance on SSO. It aims to clarify the role of the series compensation level and control parameters on SSO based on VSG control. Then, an algorithm for the parameter selection area based on the Guardian map is proposed and the area of the VSG-controlled DFIG is obtained. Finally, the accuracy and validity of the algorithm are verified by time domain simulation in MATLAB/Simulink and HIL experiment.

Keywords: doubly-fed induction generator (DFIG); sub-synchronous oscillation (SSO); virtual synchronous generator (VSG); parameter selection area

MSC: 94C60



Citation: Wang, Y.; Chen, F.; Jia, W.; Wang, R. An Algorithm for Calculating the Parameter Selection Area of a Doubly-Fed Induction Generator Based on the Guardian Map Method. *Mathematics* **2024**, *12*, 1044. <https://doi.org/10.3390/math12071044>

Received: 26 February 2024

Revised: 26 March 2024

Accepted: 28 March 2024

Published: 30 March 2024



Copyright: © 2024 by the authors. Licensee MDPI, Basel, Switzerland. This article is an open access article distributed under the terms and conditions of the Creative Commons Attribution (CC BY) license (<https://creativecommons.org/licenses/by/4.0/>).

1. Introduction

Recently, large-scale wind farms have garnered significant interest for their contribution to reducing reliance on fossil fuels. Among these, the DFIG stands out as a widely utilized wind turbine in practical applications [1,2]. Grid-connected wind power systems, being a relatively new type of power system, encounter fresh operational challenges stemming from their extensive use of power electronics [3–5]. The prevalence of issues such as low inertia and weak damping has led to several instances of instability, posing a considerable risk to the secure and stable operation of power systems [6–8].

To address these challenges effectively, VSG technology has been implemented [9,10]. In contrast to power systems predominantly governed by centralized synchronous generators (SGs), power electronics-dominated systems such as DFIG controlled by VSG may feature hundreds of distributed converters. This can result in dynamic interactions between DFIGs and

the AC grid, leading to resonance incidents that affect the safe and stable operation of wind power systems [11,12]. Furthermore, the use of VSG control complicates the mechanism of subsynchronous oscillation in wind power systems [13]. Practical engineering observations indicate that the stable operational characteristics of DFIGs are influenced by the turbine control parameters and the level of series compensation [14,15]. Large-scale DFIGs are typically connected to the grid via series compensation lines in order to enhance the transmission capacity of the AC system [16]. However, in series compensation lines, the control system of the DFIG interacts with the compensation capacitor, rendering them susceptible to subsynchronous oscillations and potentially causing large-scale off-grid scenarios [17]. Therefore, there is a pressing demand for a small-signal stability analysis method tailored to the DFIGs system. This method should both ascertain the stability conditions (whether the system is stable or unstable) and furnish solutions through parameter design-oriented stability methods. Impedance-based analysis is a proven and straightforward method for stability assessment [18–20]. Wang et al. [21] proposed a wind farm conductor and provided nodal voltage equations for the entire integrated system. Sun et al. [20] developed a model for a doubly-fed wind turbine with a multi-timescale controller, incorporating the conductance and dynamics of the dc-bus between the rotor-side converter (RSC) and the grid-side converter (GSC). Similar impedance models were developed in [22,23]. Another study [24] introduced a wind farm aggregate impedance model based on a doubly-fed converter, which accounts for nonlinearities introduced by the phase-locked loop (PLL) and external control loop of the wind converter. While this model accurately captures low-frequency dynamic interactions, it does not consider the influence of control parameters on the impedance characteristics.

Time domain modal analysis employing state-space models has been extensively utilized for decades to evaluate interactions among multiple machines and inter-area oscillations in power systems where synchronous generators (SGs) are predominant [25]. Participation factors further clarify the dynamic contributions of state variables, assisting in the control of system damping. This approach offers a comprehensive understanding of system dynamics. Through examination of the eigenvalues and eigenvectors of the state matrix, it furnishes valuable insights into oscillation modes, encompassing their frequencies, damping ratios, and mode shapes [25–28]. Despite its merits, modal analysis finds limited application in the stability assessment of large-scale power systems characterized by the prevalence of power electronics.

Efforts have been made to simplify modeling via modularizing methodology. In [29], each VSC control loop was modeled separately and then interconnected. However, integrating shared state variables among submodels within the state-space framework is essential for ensuring the accuracy of the state matrix of the system. Without clear guidelines for combining these shared variables, significant effort is required to restructure the submodels for seamless integration into the overall system representation. To address this challenge, [30] introduced principles for combining two sub-state-space models with varying interconnections. Shared state variables can be individually represented, facilitating interconnections between submodule components. This approach streamlines the process of deriving the complete system model without the need to overhaul individual submodels within the state-space framework.

The traditional state-space approach primarily aims to identify stable operating points and analyze the constraints on parameter selection using the stability criterion method [31]. However, it does not inherently provide the parameter selection area for system parameters. To address this gap, this paper introduces a modular state-space model based on the Guardian map for DFIG containing the series compensation line and solves the parameter selection area. This approach has the following main advantages:

- (1) A detailed modular model of DFIGs is proposed. Compared with [30], it focuses more on describing the operation status of DFIGs in wind farms and analyzing the structure of the modularization matrix. This is helpful in reflecting the actual situation of the wind farm and in performing the calculation of the parameter selection area.

- (2) Focusing on the investigation of the influence law of VSG control parameters on the SSO, the proposed mechanism aims to clarify the role of the series compensation level and control parameters in the subsynchronous oscillations under VSG control. This can provide guidance for system stabilization and parameter selection. Finally, the accuracy and validity of the mechanism analysis and theoretical analysis are verified by time domain simulation.

The structure of this paper is as follows: Section 2 describes the system of DFIGs and models the various parts of the system; Sections 3 and 4 describe the mathematical method of the Guardian map used to obtain the parameter selection area and develop the algorithm for DFIGs; Sections 5 and 6 provide the corresponding simulation and experimental results; and Section 7 concludes the work.

2. The Small-Signal Model of DFIG Based on VSG

The DFIG is linked to the grid via a back-to-back converter, whereby the rotor-side converter implements the VSG control strategy to regulate the output active and reactive power of DFIGs. Meanwhile, the traditional vector control strategy is retained for the grid-side converter to uphold the stability of the DC bus voltage. The influence of the converter on the overall grid-connected system is minimal. Consequently, the converter and the DC capacitor are substituted with a constant DC voltage source to simplify the analysis, disregarding the impact of the grid-side converter. This paper solely establishes the small-signal state-space model, encompassing the structure of the DFIGs, rotor-side converter, and the series complementary line. Such modeling lays the groundwork for subsequent analyses concerning the stability area of VSG-controlled DFIG units connected to the grid via a series compensation line.

2.1. Stator and Rotor Models of DFIG

The DFIG is split into two components: the rotor and the stator. The equivalent structural block diagrams for both the stator and rotor sides are depicted in Figure 1. It is specified that the inflow current is directed positively on both the stator and rotor sides.

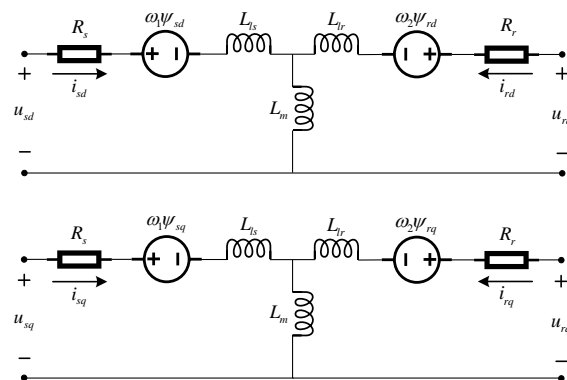


Figure 1. Block diagram of stator and rotor structure of DFIG.

The voltage equation and the linkage equation of a DFIG in the $d - q$ coordinate system can be represented as follows:

$$\begin{cases} u_{sd} = R_s i_{sd} - \omega_1 \psi_{sq} + \frac{d\psi_{sd}}{dt} \\ u_{sq} = R_s i_{sq} + \omega_1 \psi_{sd} + \frac{d\psi_{sq}}{dt} \\ u_{rd} = R_r i_{rd} - \omega_2 \psi_{rq} + \frac{d\psi_{rd}}{dt} \\ u_{rq} = R_r i_{rq} + \omega_2 \psi_{rd} + \frac{d\psi_{rq}}{dt} \end{cases} \quad (1)$$

Active power control means that the deviation of the output active power from the given active power is controlled by inertia and damping to obtain the rotor excitation voltage phase angle. Its control equation can be expressed as follows:

$$\begin{cases} T_j \frac{d\omega_{vsg}}{dt} = P_{s-ref} - P_s - D(\omega_{vsg} - \omega_1) \\ \frac{d\theta_r}{dt} = \omega_b(\omega_{vsg} - \omega_r) \end{cases} \quad (6)$$

Introducing the intermediate variables x_1, x_2 , Equation (6) can be expressed as follows:

$$\begin{cases} \frac{dx_1}{dt} = P_{s-ref} - P_s - D(\omega_{vsg} - \omega_1) \\ \frac{dx_2}{dt} = \omega_{vsg} - \omega_r \\ \omega_{vsg} = x_1 / T_j \\ \theta_r = \omega_b x_2 \end{cases} \quad (7)$$

Reactive power control means that the deviation of the actual output reactive power from the given reference value of the reactive power is used to obtain the rotor excitation voltage amplitude through PI control. The control equation can be expressed as follows:

$$U_r = (k_{pv} + \frac{k_{iv}}{s})(Q_{s-ref} - Q_s). \quad (8)$$

Introducing the intermediate variable x_3 , Equation (8) can be expressed as

$$\begin{cases} \frac{dx_3}{dt} = Q_{s-ref} - Q_s \\ U_r = k_{pv} \frac{dx_3}{dt} + k_{iv} x_3 \end{cases} \quad (9)$$

Finally, the excitation control voltage U_{r-abc} of the rotor in the three-phase stationary coordinate system can be obtained by vector synthesis, i.e.,

$$U_{rabc} = \frac{2}{3}(U_{ra} + e^{j\frac{2}{3}\pi}U_{rb} + e^{j\frac{4}{3}\pi}U_{rc}), \quad (10)$$

where $U_{ra} = U_r \cos(\theta_r)$, $U_{rb} = U_r \cos(\theta_r - \frac{2}{3}\pi)$, and $U_{rc} = U_r \cos(\theta_r - \frac{4}{3}\pi)$.

The controller output is transformed from a three-phase stationary coordinate system to a $d-q$ coordinate system. It can be obtained as follows:

$$\begin{cases} u_{rd} = U_r \cos \theta_r \\ u_{rq} = U_r \sin \theta_r \end{cases} \quad (11)$$

The small-signal linearization of Equation (11) yields

$$\begin{cases} \Delta u_{rd} = -U_{r0} \sin \theta_{r0} \Delta \theta_r + \cos \theta_{r0} \Delta U_r \\ \Delta u_{rq} = U_{r0} \cos \theta_{r0} \Delta \theta_r + \sin \theta_{r0} \Delta U_r \end{cases} \quad (12)$$

Based on Equations (7) and (9) above, the VSG control can be expressed as a third-order state equation, and its small-signal linearization yields

$$\begin{cases} \frac{d\Delta x_1}{dt} = -\Delta P_s - D\Delta \omega_{vsg} \\ \frac{d\Delta x_2}{dt} = \Delta \omega_{vsg} \\ \frac{d\Delta x_3}{dt} = -\Delta Q_s \end{cases} \quad (13)$$

where the expressions for active and reactive power are

$$\begin{cases} P_s = 1.5(U_{sd}I_{sd} + U_{sq}I_{sq}) \\ Q_s = 1.5(U_{sq}I_{sd} - U_{sd}I_{sq}) \end{cases} \quad (14)$$

The small-signal linearization of this can be expressed as follows:

$$\begin{cases} \Delta P_s = 1.5(U_{sd0}\Delta i_{sd} + U_{sq0}\Delta i_{sq} + I_{sd0}\Delta u_{sd} + I_{sq0}\Delta u_{sq}) \\ \Delta Q_s = 1.5(U_{sq0}\Delta i_{sd} - U_{sd0}\Delta i_{sq} + I_{sd0}\Delta u_{sq} - I_{sq0}\Delta u_{sd}) \end{cases} \quad (15)$$

The virtual angular frequency and rotor excitation voltage phase angle in Equation (7) can be expressed after small-signal linearization as

$$\begin{cases} \Delta\omega_{vsg} = \Delta x_1/T_j \\ \Delta\theta_r = \omega_b\Delta x_2 \end{cases} \quad (16)$$

Then, the output rotor voltage amplitude can be expressed as

$$\Delta U_r = 1.5k_{pr}(U_{sq0}\Delta i_{sd} - U_{sd0}\Delta i_{sq} + I_{sd0}\Delta u_{sq} - I_{sq0}\Delta u_{sd}) + k_{iv}\Delta x_3. \quad (17)$$

Thus the small-signal expression for the output rotor voltage in the $d-q$ coordinate system can be obtained as follows:

$$\begin{cases} \Delta u_{rd} = -U_{r0} \sin \theta_{r0} a_\theta \Delta x_2 + k_{r0} \cos \theta_{r0} \Delta x_3 \\ \quad + 1.5k_{pn} \cos \theta_{r0} (U_{sq0}\Delta i_{sd} - U_{sd0}\Delta i_{sq} + I_{sd0}\Delta u_{sq} - I_{sq0}\Delta u_{sd}) \\ \Delta u_{rq} = U_{r0} \cos \theta_{r0} \omega_b \Delta x_2 + k_r \sin \theta_{r0} \Delta x_3 \\ \quad + 1.5k_{pn} \sin \theta_{r0} (U_{sq0}\Delta i_{sd} - U_{sd0}\Delta i_{sq} + I_{sd0}\Delta u_{sq} - I_{sq0}\Delta u_{sd}) \end{cases} \quad (18)$$

Combining Equations (12)–(18), the state-space equations for VSG control can be expressed as follows:

$$\frac{d}{dt} \begin{bmatrix} \Delta x_1 \\ \Delta x_2 \\ \Delta x_3 \end{bmatrix} = A_{VSG} \begin{bmatrix} \Delta x_1 \\ \Delta x_2 \\ \Delta x_3 \end{bmatrix} + B_{VSG1} \begin{bmatrix} \Delta i_{sd} \\ \Delta i_{sq} \end{bmatrix} + B_{VSG2} \begin{bmatrix} \Delta u_{sd} \\ \Delta u_{sq} \end{bmatrix} \quad (19)$$

$$\text{where } A_{VSG} = \begin{bmatrix} -D/T_j & 0 & 0 \\ 1/T_j & 0 & 0 \\ 0 & 0 & 0 \end{bmatrix}, B_{VSG1} = \begin{bmatrix} 1.5U_{sd0} & 1.5U_{sq0} \\ 0 & 0 \\ 1.5U_{sq0} & -1.5U_{sd0} \end{bmatrix},$$

$$B_{VSG2} = \begin{bmatrix} 1.5I_{sd0} & 1.5I_{sq0} \\ 0 & 0 \\ -1.5I_{sq0} & 1.5I_{sd0} \end{bmatrix}.$$

2.3. Complete Model of a DFIG with the Series-Complementary Line

DFIGs are generally located in remote areas; in order to reduce the transmission line impedance when accessing the grid, they are often accessed through series compensation capacitors. However, the output impedance of DFIGs is often inductive, which is prone to resonance with capacitive transmission lines, i.e., the SSR phenomenon. Therefore, in order to analyze the grid stability of doubly-fed wind turbines under a series compensation grid, it is necessary to analyze the turbine together with the transmission line model. The small-signal state-space model of the DFIG, rotor-side converter, and its controller have been established in the previous section. The transmission line model is established in the following section to form the complete state-space model of a VSG-controlled DFIG under a series compensation line to analyze the stability of the grid-connected system.

The simplified structural block diagram of the DFIG connected to the grid by the series compensation line is shown in Figure 3; the voltage–current relationship of line resistance, inductance, and capacitance can be expressed as follows:

$$\begin{cases} u_{sd} - u_{gd} + u_{cd} = \omega_1 L_g i_{sq} - R_g i_{gd} - L_g \frac{di_{sd}}{dt} \\ u_{sq} - u_{sg} + u_{cq} = -\omega_1 L_g i_{sd} - R_g i_{sq} - L_g \frac{di_{sq}}{dt} \\ C_g \frac{du_{cd}}{dt} = i_{sd} + \omega_1 C_g u_{cq} \\ C_g \frac{du_{cq}}{dt} = i_{sq} - \omega_1 C_g u_{cd} \end{cases} \quad (20)$$

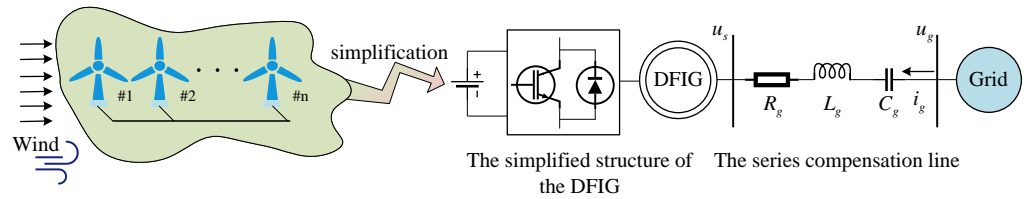


Figure 3. Block diagram of DFIG connected to the grid via series complementary capacitors.

The small-signal expression of Equation (20) can be expressed as follows:

$$\begin{cases} \Delta u_{sd} + \Delta u_{cd} = \omega_1 L_g \Delta i_{sq} - R_g \Delta i_{sd} - L_g \frac{d\Delta i_{sd}}{dt} \\ \Delta u_{sq} + \Delta u_{cq} = -\omega_1 L_g \Delta i_{sd} - R_g \Delta i_{sq} - L_g \frac{d\Delta i_{sq}}{dt} \\ C_g \frac{d\Delta u_{cd}}{dt} = \Delta i_{sd} + \omega_1 C_g \Delta u_{cq} \\ C_g \frac{d\Delta u_{cq}}{dt} = \Delta i_{sq} - \omega_1 C_g \Delta u_{cd} \end{cases} \quad (21)$$

Because the grid-side converter along with its controller and DC bus capacitor are replaced by a voltage source, only the rotor-side converter with VSG control is considered for the DFIG system. At this time, the line current and the stator output current of the DFIG are equal, i.e., $i_{gd} = i_{sd}$, $i_{gq} = i_{sq}$.

Thus, Equation (21) can be written in the following form:

$$\frac{d}{dt} \begin{bmatrix} \Delta u_{cd} \\ \Delta u_{cq} \end{bmatrix} = \begin{bmatrix} \frac{1}{C_g} & 0 \\ 0 & \frac{1}{C_g} \end{bmatrix} \begin{bmatrix} \Delta i_{sd} \\ \Delta i_{sq} \end{bmatrix} + \begin{bmatrix} 0 & \omega_1 \\ -\omega_1 & 0 \end{bmatrix} \begin{bmatrix} \Delta u_{cd} \\ \Delta u_{cq} \end{bmatrix} \quad (22)$$

$$\frac{d}{dt} \begin{bmatrix} \Delta i_{sd} \\ \Delta i_{sq} \end{bmatrix} = \begin{bmatrix} \frac{-1}{L_g} & 0 \\ 0 & \frac{-1}{L_g} \end{bmatrix} \begin{bmatrix} \Delta u_{sd} \\ \Delta u_{sq} \end{bmatrix} + \begin{bmatrix} \frac{-R_g}{L_g} & \omega_1 \\ -\omega_1 & \frac{-R_g}{L_g} \end{bmatrix} \begin{bmatrix} \Delta i_{sd} \\ \Delta i_{sq} \end{bmatrix} + \begin{bmatrix} \frac{-1}{L_g} & 0 \\ 0 & \frac{-1}{L_g} \end{bmatrix} \begin{bmatrix} \Delta u_{cd} \\ \Delta u_{cq} \end{bmatrix}. \quad (23)$$

Equations (5), (18), (19), (22), and (23) are associated, and the inputs are substituted equivalently. Thus, the standard small-signal state-space equation for n DFIGs containing the series compensation line is as follows:

$$\frac{d\Delta x_{sys}}{dt} = A_{sys} \Delta x_{sys}, \quad (24)$$

where the state variables are denoted as Δx_{sys} , T_{sys} is the characterization matrix of the system, and the series compensation stability of the DFIG system can be determined by

solving the eigenvalues of this characterization matrix. The structure of T_{sys} and Δx_{sys} is shown in Figure 4.

$$\Delta x_{sys} = [\Delta i_{rd}^1 \quad \Delta i_{rq}^1 \quad \Delta i_{sd}^1 \quad \Delta i_{sq}^1 \quad \Delta x_1^1 \quad \Delta x_2^1 \quad \Delta x_3^1 \quad \Delta i_{rd}^2 \quad \Delta i_{rq}^2 \quad \Delta i_{sd}^2 \quad \Delta i_{sq}^2 \quad \Delta x_1^2 \quad \Delta x_2^2 \quad \Delta x_3^2 \quad \dots \quad \Delta i_{rd}^n \quad \Delta i_{rq}^n \quad \Delta i_{sd}^n \quad \Delta i_{sq}^n \quad \Delta x_1^n \quad \Delta x_2^n \quad \Delta x_3^n \quad \Delta u_{cd} \quad \Delta u_{cq}]^T \quad (25)$$

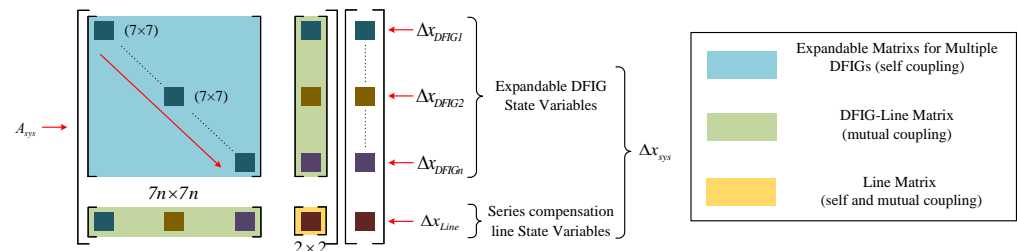


Figure 4. The structures of A_{sys} and Δx_{sys} .

3. The Parameter Selection Area

At the point of equilibrium, the small-signal model of the system can be characterized as follows:

$$\Delta \dot{x}_{sys} = A_{sys}(\rho) \Delta x_{sys} \quad (26)$$

System stability is determined by ensuring that the real parts of all eigenvalues are negative. The parameter selection significantly influences system stability. However, if damping is insufficient and the oscillatory decay coefficient is minimal, instability can arise despite the system being theoretically stable. Weak damping can lead the system close to instability, making it prone to oscillations when perturbed. Thus, to prevent SSO induced by the series compensation line, the eigenvalue vector of the DFIG system is manipulated accordingly, denoted as follows:

$$\lambda = [\lambda_1, \lambda_2, \dots, \lambda_i, \dots, \lambda_n]. \quad (27)$$

The eigenvalues are expressed as $\lambda_i = a_i + b_i j$, where a_i represents the real part and b_i denotes the imaginary part of each eigenvalue.

The parameter selection area is described as the set of DFIGs that meet the following two criteria:

Criterion I: The real part of the system's eigenvalue a_i , determined by the attenuation coefficient $\leq -\nu_1$, where ν_1 is a positive value.

Criterion II: The system's damping ratio $\leq \nu_2$, where $\nu_2 = \sin(\theta)$ and θ represents an angle.

The damping ratio is defined as ξ_i :

$$\xi_i = \frac{-a_i}{\sqrt{a_i^2 + b_i^2}}. \quad (28)$$

Figure 5 illustrates the boundaries of the parameter selection area, which are established according to two criteria. Criterion I delineates the limits for the real parts of the system's eigenvalues, ensuring stability and rapid oscillatory decay, while Criterion II establishes the threshold for the damping ratio at each stable operating point.

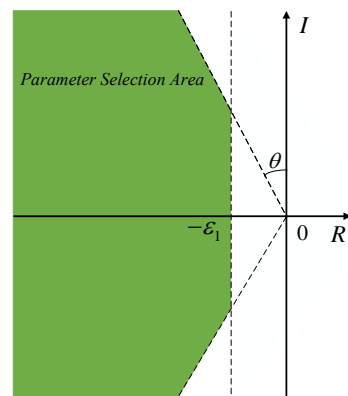


Figure 5. The parameter selection area and its complex plane boundary.

The Guardian map method for identifying parameter selection areas is restricted to systems with stable matrices, where all the eigenvalues possess negative real parts. Adapting this method for irregular regions such as the parameter selection area requires mapping the negative half-plane onto the target region. This process entails subdividing the area and identifying their intersections with the mapping, as illustrated in Figure 6. If the eigenvalue set of the target system matrix falls within Area 1, it corresponds to Criterion I. Alternatively, if it falls within Area 2 or Area 3, it aligns with Criterion II.

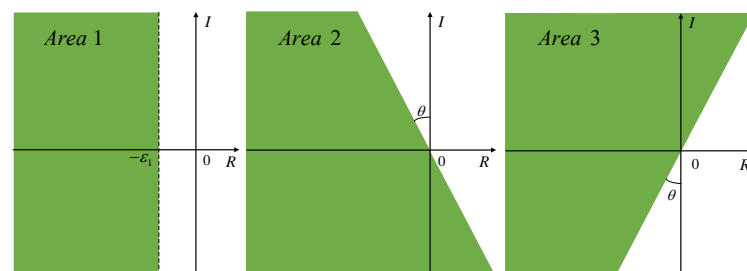


Figure 6. Decomposition of the parameter selection area.

To project the negative side onto Area 1, the transformation is represented as follows:

$$v_1 : A_{translation} = A_{left} + \varepsilon_1 E \quad (29)$$

where A_{left} stands for a fixed matrix with no variables, $A_{translation}$ denotes the translation transformation of the matrix stability region for this system, and E indicates the identity matrix.

To project the negative side onto Areas 2 and 3, the rotations are indicated as follows:

$$v_2 : A_{rotation1} = A_{left} \times e^{i\theta}, \quad (30)$$

$$v_3 : A_{rotation2} = A_{left} \times e^{-i\theta}, \quad (31)$$

where $A_{rotation1}$ and $A_{rotation2}$ correspondingly represent two rotations in the clockwise and counterclockwise directions within the selection region and θ denotes the angle of rotation.

When $A_{translation}$, $A_{rotation1}$, and $A_{rotation2}$ have been acquired, the method for calculating the parameter selection region using Guardian mapping can be utilized to identify the respective regions. The region targeted in this study is the overlapping part of the three regions fulfilling the aforementioned two stability criteria.

4. Algorithm for the Parameter Selection Area of DFIGs

In this section, an algorithm is introduced for determining the parameter selection region for DFIGs. Expanding upon the earlier discussion, it is demonstrated that if the $A_{translation}$, $A_{rotation1}$, and $A_{rotation2}$ respectively produced from the translation and two rotation mappings yield Hurwitz matrices, then the system will uphold its stability and

demonstrate favorable performance attributes. Additionally, identifying the stable operational region can be reframed as a problem of identifying an associated Hurwitz matrix.

In the preceding section, the multiparameter state-space matrix ($A_{translation}$, $A_{rotation1}$, and $A_{rotation2}$) can be represented as

$$A_{sys} = A_{sys}(\rho_1, \rho_2, \dots, \rho_m) = A_0 + \rho_i \sum_{i=1}^m A_{sys,i}, \quad (32)$$

where $\rho_1, \rho_2, \dots, \rho_m$ denote the variation coefficients, A_0 represents the fixed matrix without fluctuations in parameters, and $T_{g,i}$ stands for the transformation matrix influenced by the fluctuations ρ_i .

To streamline the variables in Equation (32), the issue can be resolved by employing the polar coordinate transformation technique outlined in Lemma 1.

Lemma 1 ([32]). *Considering a vector $(\rho_1, \rho_2, \dots, \rho_m)^T \in U^m$ with $m \geq 2$, there exist two real numbers r and $m - 1$ scalar quantities, satisfying the following conditions:*

$$(\rho_1, \rho_2, \dots, \rho_m)^T = r\kappa(\theta) \quad (33)$$

where $\theta = (\theta_2, \dots, \theta_m)^T \in [0, \pi)^{m-1}$ and

$$\begin{aligned} \kappa(\theta) &= (\cos \theta_2, \cos \theta_3 \sin \theta_2, \cos \theta_4 \sin \theta_3 \sin \theta_2, \dots, \\ &\cos \theta_{m-1} \dots \sin \theta_3 \sin \theta_2, \cos \theta_k \dots \sin \theta_3 \sin \theta_2)^T \in [-1, 1]^m \end{aligned} \quad (34)$$

Utilizing Lemma 1, the multi-parameter system matrix can be condensed to

$$A_{sys} = A_0 + rT_{\kappa(\theta)}. \quad (35)$$

Theorem 1. *Given an open range T_0 , where $A_{\kappa(\theta)} \subseteq \Omega$ and $\bar{A}_0 \neq 0$, let $\bar{A}_0 \triangleq 2A_0 \odot E$ and $\bar{A}_{\kappa(\theta)} \triangleq 2A_{\kappa(\theta)} \odot E$. Then, for all $r \in U$ and $0 \in U$ such that $A_{sys} = A_0 + rA_{\kappa(\theta)}$ forms a Hurwitz matrix, the necessary and sufficient conditions are that A_0 is a Hurwitz matrix and $0 \in U \in \Phi(A_0^{-1}A_{\kappa(\theta)}) \cap \Phi(\bar{A}_0^{-1}\bar{A}_{\kappa(\theta)})$.*

The proof of Theorem 1 has been established in [33] and will not be reiterated in this paper.

Consider the set defined as follows:

$$\Omega(\theta) = \bigcup_{i \in \Gamma(\theta)} (r_i, r_{i+1}), \quad (36)$$

where r_i and r_{i+1} respectively represent consecutive elements within $\Phi(\bar{A}_0^{-1}\bar{A}_{\kappa(\theta)})$ with $i \in [0, 1, \dots, m-1, m]$ and $\Gamma(\theta)$ denotes an index set $\Gamma(\theta) = i : \text{For } r_i' \in (r_i, r_{i+1})$. Here, $A_0 + r_i' A_{\kappa(\theta)}$ is assumed to be a Hurwitz matrix. The delineation of the system parameter's selection area is elaborated further as follows:

$$\Gamma'_{\in}(\theta) = \left\{ \bigcup_{\theta \in [0, \pi)^{m-1}} \{v(\theta) \in U^m : v(\theta) = r\kappa(\theta), r \in \Gamma_{\in}(\theta)\} \right\}. \quad (37)$$

Only when $(r_1, r_2, \dots, r_m)^T \in \Gamma'_{\in}(\theta)$ does $A_0 + r_i \sum_{i=1}^m A_{sys,i}$ form a Hurwitz matrix.

Given Equation (32), the small-signal state-space matrix represents a linear relationship with the parameters. Hence, Algorithm 1 provides the solution process for determining the parameter selection area of C_g and k_{iv} .

Algorithm 1 The parameter selection area of C_g and k_{iv} .

- 1: **Initialization:** U_1 is the universal set, $A_{sys} = A_{translation}$.
- 2: **while** ($i \leq p$) **do**
- 3: Utilize the current stable operating point to conduct small-signal expansion, yielding the stable matrix A_0 and the perturbation matrix $A_{sys,i}$ consisting of C_g and k_{iv} .
- 4: Define $C_g = r \sin(\theta)$; $k_{iv} = r \cos(\theta)$, and simplify the system matrix into the form $A_{sys} = A_0 + rA_{\kappa(\theta)}$.
- 5: Compute the eigenvalues of \bar{A}_0 , $\bar{A}_{\kappa(\theta)}$, and $\bar{A}_0^{-1}\bar{A}_{\kappa(\theta)}$, where $\theta \in [0, \frac{\pi}{2}]$
- 6: Establish $\Omega(\theta) = (r_0, r_1, \dots, r_{k+1})$ according to the Definition.
- 7: For each $r'_i \in (r_i, r_{i+1})$, verify whether the matrix $A_0 + r'_i A_{\kappa(\theta)}$ forms a Hurwitz matrix. If affirmative, the system within this open range maintains stability.
- 8: Aggregate all stable open intervals $U_1 = U_1 \cup U_{1i}$ to obtain the stability domain U_{1i} of the control parameters.
- 9: Increment i by one.
- 10: **end while**

Illustrated in Figure 7 is the execution flow of the parameter selection area. First, the setup initializes the initial conditions. Subsequently, it iterates through calculating the system's steady-state matrix and perturbation matrix, simplifying the system matrix, computing the eigenvalues, constructing the ensemble, and checking the system stability. System stability is assessed based on the fulfillment of the Hurwitz matrix conditions, and stable parameter intervals are appended to the set. This loop continues until all parameter combinations are checked, resulting in the stable parameter set. Moreover, Algorithm 1 allows the parameter selection areas U_2 and U_3 to be derived using matrices $A_{rotation1}$ and $A_{rotation2}$. Consequently, the parameter selection area is expressed as the intersection of U_1 , U_2 , and U_3 , denoted as $U = U_1 \cap U_2 \cap U_3$.

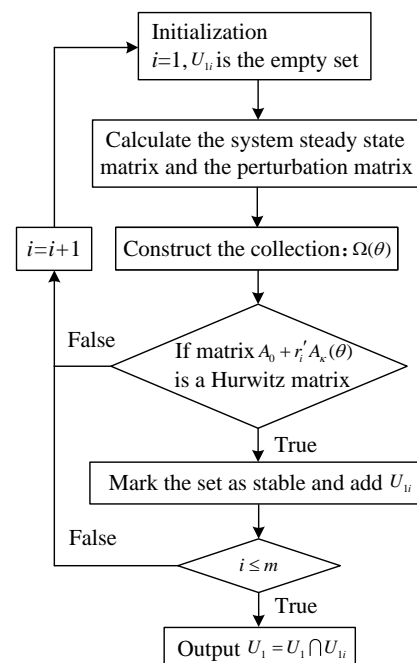


Figure 7. The computational flow of the algorithm in calculating the DFIG parameter selection area based on the Guardian map.

5. Simulation Experiments

The computational example in this paper uses a grid-connected wind farm system containing three DFIGs with the parameters shown in Table 1 and the other parameters in [34]. In the initial state, each DFIG has the same parameter settings and all of them operate at the unit power factor. The correctness of the theoretical derivation in Section 4 of this paper is verified by model analysis and time domain simulation.

Table 1. Simulation parameters of DFIG and grid line.

Parameters	Symbols	Values
DFIG parameters		
Rated voltage	U_b	690 V
Rotor resistance	R_r	0.081 pu
Rotor leakage inductance	L_r	0.75 pu
Excitation inductance	L_m	17.21 pu
Active power	P_s	100 MW
Reactive power	Q_s	0 MW
DC voltage	U_{dc}	1150 V
Stator resistance	R_s	0.092 pu
Stator leakage inductance	L_s	0.45 pu
VSG control parameters		
Rated Voltage	T_j	0.5
Rotor resistance	D	20
Rotor leakage inductance	k_{pv}	30
Excitation inductance	k_{iv}	5
Grid line parameters		
Grid resistance	R_g	0.1 pu
Grid Inductance	L_g	2 pu
Compensation Capacitance	C_g	3.5 pu

5.1. Validation of the Root-Locus in the Parameter Selection Area

First, the study was carried out in an ideal situation where the wind farm parameter settings and operating conditions are exactly the same. A detailed electromagnetic transient time domain simulation model was built in MATLAB/SIMULINK to verify the results of the model analysis. As the parameters of each DFIG are the same, the small differences in the DFIG inlet currents and voltages are ignored. The output voltage, output current, active power, reactive power voltage, and DC port voltage waveforms of the DFIG in the initial state are shown in Figure 8, respectively. According to the simulation results, the system under the series compensation capacitance value $C_g = 3.5$ pu and the integral coefficient $k_{iv} = 10$ is shown to be stable. As shown in Figure 9, the parameter selection area is calculated from Algorithm 1, provided in Section 4. Because the parameter coordinates at this point are located within the selection area, the system is judged to be stable according to the methodology of this paper. This result is the same as the simulation results. Furthermore, the operating points of the system located in the parameter stabilization region are drawn in the figure using the point-by-point test method (indicated by the blue “*”). The accuracy of the strategy proposed in this paper is confirmed by the fact that almost all of the test points are located within the range of the parameter selection area.

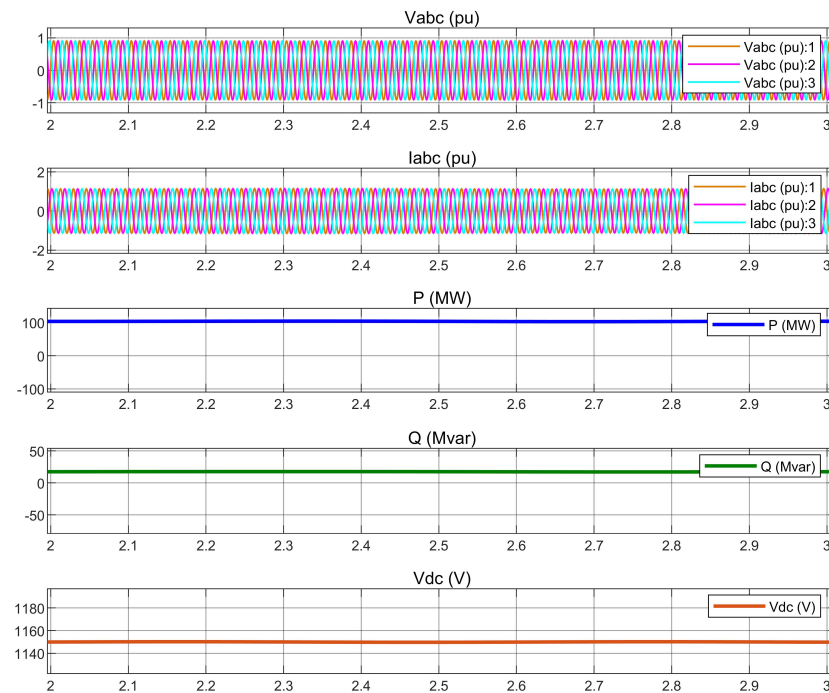


Figure 8. The time domain simulation result for initial state $((C_g, k_{iv}) = (3.5 \text{ pu}, 10))$.

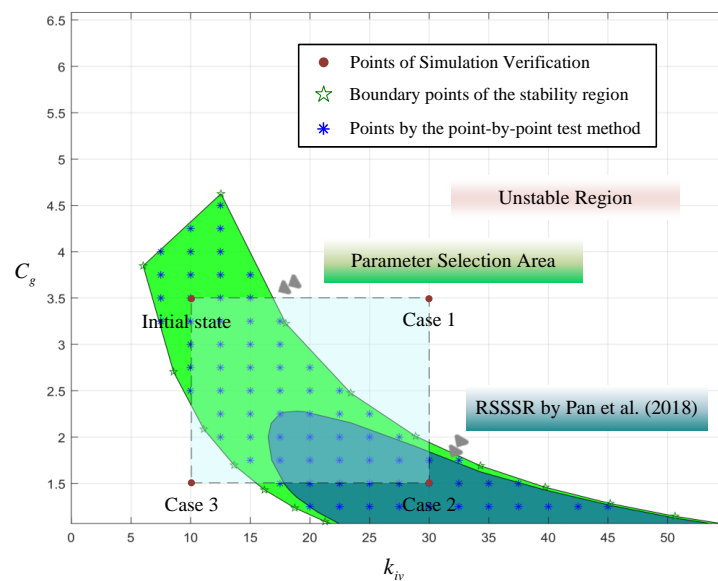


Figure 9. The parameter selection area of C_g and k_{iv} [35].

In order to verify the correctness of the theoretical approach in this paper, the corresponding 23×23 order model of the example system in Figure 3 was constructed and the oscillation mode of the full-order model was calculated. The value of the series compensation capacitor C_g was varied in the range of 3.5 pu 1 pu, while the rest of the parameters remained unchanged. The root-locus of the model at this point was calculated, as shown in Figure 10a. From the figure, it is evident that as the value of the series compensation capacitance (denoted as the series compensation coefficient) increases, the $\lambda_{2,3}$ mode shifts towards the right half-plane, indicating a tendency towards system instability coupled with an increase in oscillation frequency. This correlation is validated by the time domain simulation results depicted in Figure 10c. The alterations in the output power waveform of the system are observed with series compensation capacitor values of 3.5 pu, 2.5 pu, and 1 pu, respectively. Notably, a lower C_g results in more pronounced oscillations in the

output power waveform of the system and is accompanied by a significant increase in oscillation frequency, consistent with the characteristics observed in the eigenvalue analysis. Consequently, it can be inferred that as the series compensation capacitance decreases, signifying an increase in the series compensation level, the control bandwidth decreases as well, leading to heightened system oscillations.

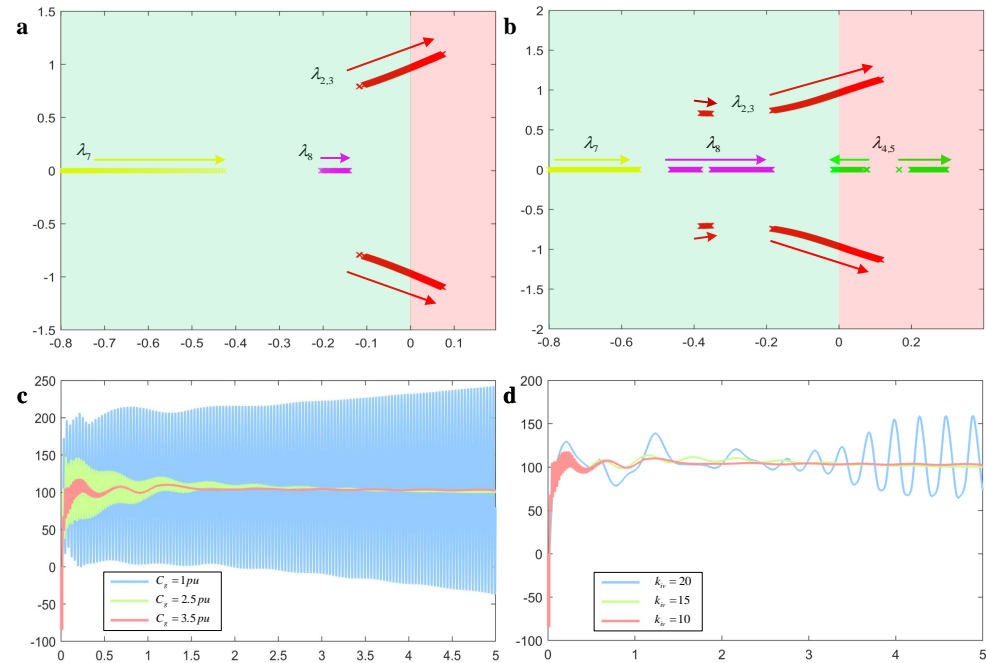


Figure 10. The root-locus and output active power waveforms when parameters are changed. (a) the root-locus when C_g decrease from 3.5 pu to 1 pu; (b) The root-locus when k_{iv} increase from 10 to 20; (c) the output active power waveforms for $C_g = 1$ pu, 2.5 pu, 3.5 pu; and (d) the output active power waveforms for $k_{iv} = 20, 15, 10$.

We next set the integration gain K_{iv} of the reactive power loop to vary from 10 to 20 while keeping the rest of the parameters unchanged and calculated the root-locus of the model at this time, as shown in Figure 10b. From the figure, it is apparent that as the integral gain increases, the stability of the $\lambda_{2,3}$ mode weakens, accompanied by an increase in the oscillation frequency. Additionally, there are $\lambda_{4,5}$ modes that shift towards the right with the increasing integral gain, positioning themselves on the right side of the imaginary axis. Subsequent time domain simulation validated the aforementioned observations. The changes in the output active power waveform of the system when setting the integral gain to 10, 15, and 20, respectively, are depicted in Figure 10d. Notably, the oscillation of the output power waveform of the system becomes more pronounced with larger integral gain values, aligning with the characteristic root trend. Hence, it can be inferred that the system tends towards destabilization as the integral gain of the reactive power loop increases.

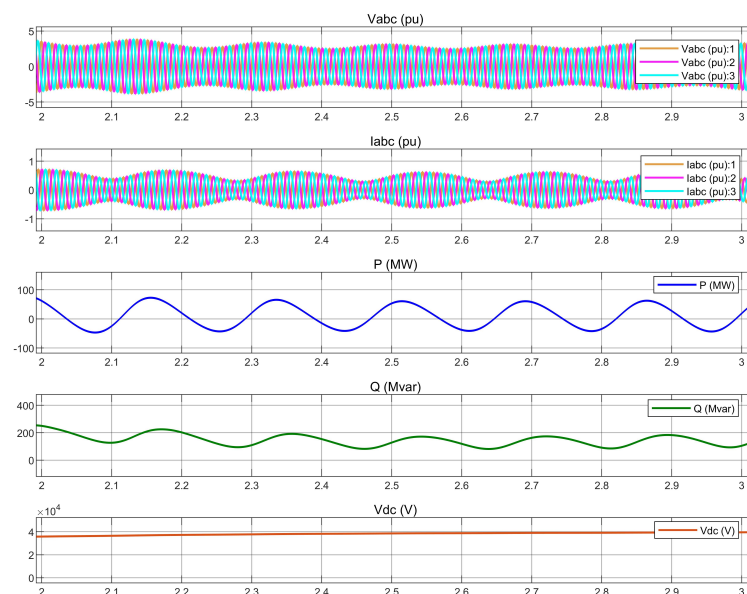
5.2. Validation of the Nonlinear Simulation in the Parameter Selection Area

The validity of the proposed method was further verified under different operating conditions and different turbine parameter settings. Table 2 provides the results of the parameter coordinates (C_g, k_{iv}) and the numerical analysis method when the DFIG operating parameters C_g and k_{iv} were changed. The position of each parameter is labeled in the selection area of Figure 9.

Table 2. Results of the numerical analysis of the four cases.

Situations	(C_g, k_{iv})	Whether in the Stability Region	Oscillation Mode	Attenuation Coefficient	The Damping Ratio
Initial state	(3.5, 10)	YES	$-0.12 \pm 0.72i$	0.12	0.2252
Case 1	(3.5, 30)	NO	$0.17 \pm 1.54i$	NONE	NONE
Case 2	(1.5, 30)	YES	$-0.24 \pm 0.53i$	-0.24	0.709
Case 3	(1.5, 10)	NO	$0.05 \pm 0.98i$	NONE	NONE

The modeling approach for the parameters outlined in the table above aligns with the findings of the parameter selection area analysis. This demonstrates that the proposed method accurately assesses the small-signal stability of the DFIG across varying parameters. Moreover, based on the distribution of the four-parameter settings within the selection area, as illustrated in Figure 11, it is evident that the initial state and case 2 both reside within the selection area, whereas case 1 and case 3 are located outside the selection area. Consequently, the method proposed in this study can effectively evaluate the risk of instability and the stability margin of the DFIG under diverse parameter configurations, offering valuable guidance for parameter adjustment. Figures 11–13 depict the time domain simulation results for the three parameter values corresponding to case 1, case 2, and case 3, representing the three states of system instability, stability, and instability, respectively. Moreover, the initial conditions are stable but not within the RSSR of [35]. Therefore, the method of calculating the parameter selection area in this paper has low conservatism. The algorithm expands the parameter selection area as much as possible to improve flexibility while ensuring its stability.

**Figure 11.** Time domain simulation result for case 1 ($(C_g, k_{iv}) = (3.5 \text{ pu}, 30)$).

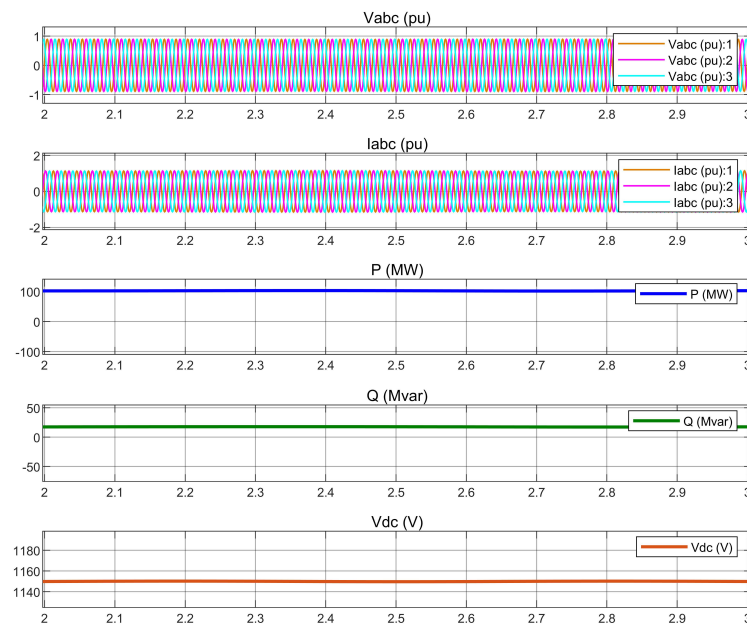


Figure 12. Time domain simulation result for case 2 ($(C_g, k_{iv}) = (1.5 \text{ pu}, 30)$).

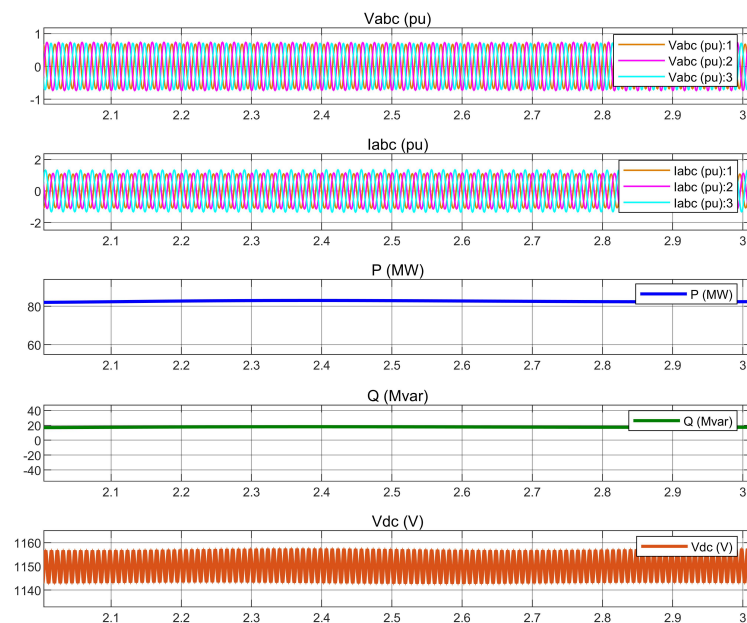


Figure 13. Time domain simulation result for case 3 ($(C_g, k_{iv}) = (1.5 \text{ pu}, 10)$).

By comparing Figures 11–13, it is evident that the stability outcomes from nonlinear simulation mirror those obtained from the stability analysis. This further substantiates the accuracy of the parameter selection area algorithm proposed in this paper.

6. HIL Experiments

The effectiveness of the proposed method for computing the DFIG parameter selection area was further validated experimentally. Hardware-in-the-loop (HIL) experiments were conducted utilizing a setup comprising a PC host computer, DSP controller, NI PXIe-1082, and oscilloscope. The core of the hardware control system is the NI real-time simulator, which handles sensor signal processing and control command execution. Specifically, the NI PXIe-1082 operates the power system. Meanwhile, the DSP controller executes the control algorithm for the power system. The PC host computer is responsible for developing simulation control strategies and constructing the main circuit for the power

system. It establishes connections with the DSP controller and the NI real-time simulator, as illustrated in Figure 14, facilitating the transfer of control algorithms to the DSP and power circuit configurations to the NI simulator.

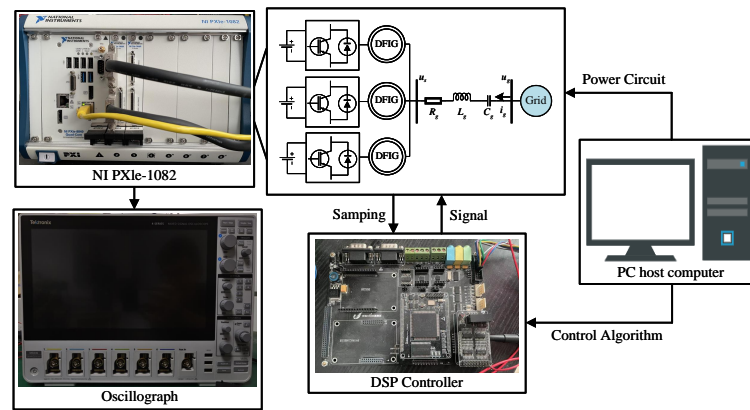


Figure 14. The experimental setup.

Initially, the series compensation level and control parameter were the same as in Section 5. The area of C_g and k_{iv} is illustrated in Figure 9, where the green domain indicates system stability. For the selected parameters $((C_g, k_{iv}) = (3.5 \text{ pu}, 10))$, the DFIGs system is stable, as demonstrated by the stable AC voltage and current in Figure 15a; however, when the parameters are changed to $((C_g, k_{iv}) = (3.5 \text{ pu}, 30))$ and $((C_g, k_{iv}) = (1.5 \text{ pu}, 10))$, the DFIGs system becomes unstable, as shown in Figure 15b,c. These experimental results confirm that the system remains stable when the series compensation level and control parameter fall within the parameter selection area, and that it can become unstable when the parameters lie outside this area. Moreover, in the conservativeness verification, $((C_g, k_{iv}) = (3.5 \text{ pu}, 10))$, $((C_g, k_{iv}) = (3.5 \text{ pu}, 30))$ and $((C_g, k_{iv}) = (1.5 \text{ pu}, 10))$ are not within the RSSR of [35]. However, $((C_g, k_{iv}) = (3.5 \text{ pu}, 10))$ is stabilized in the HIL experiment. Compared with other benchmark algorithms, this paper's algorithm for calculating the parameter selection area has lower conservativeness. In the accuracy verification, only $((C_g, k_{iv}) = (3.5 \text{ pu}, 10))$ is located within the area where neither $((C_g, k_{iv}) = (3.5 \text{ pu}, 30))$ nor $((C_g, k_{iv}) = (1.5 \text{ pu}, 10))$ are located in the point-by-point testing method. The stable operation of $((C_g, k_{iv}) = (3.5 \text{ pu}, 10))$ in the experimental results confirms the accuracy of the algorithm. In conclusion, the conservativeness and accuracy of the algorithm are well verified. The algorithm provides valuable guidance for selecting appropriate series compensation levels and control parameters in real-time applications.

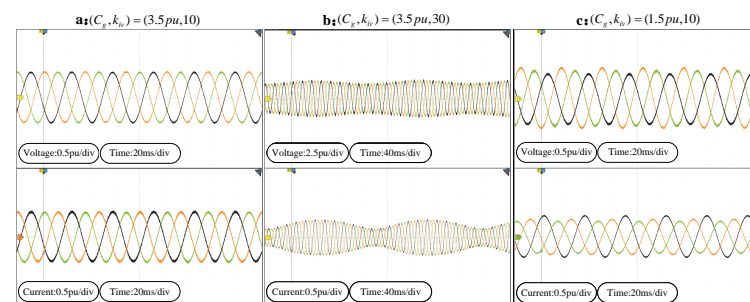


Figure 15. HIL experimental results: (a) output voltage and current waveforms for $C_g = 3.5 \text{ pu}$ $k_{iv} = 10$; (b) output voltage and current waveforms for $C_g = 3.5 \text{ pu}$ $k_{iv} = 30$; and (c) output voltage and current waveforms for $C_g = 1.5 \text{ pu}$ $k_{iv} = 10$.

7. Conclusions

Over the past several years, a series of unstable events have occurred in grid-connected wind power systems, posing a significant threat to the safe and stable operation of power grids. To counteract or alleviate the system stability issues arising from grid-connected wind

power, it is imperative to develop effective analysis methods and accurately characterize the parameter selection area of the system. This paper introduces a modular state-space model based on the Guardian map for DFIGs containing series compensation lines and solves the problem of quantitative analysis of the parameter selection area. First, a detailed modular state-space model for VSG control is established. The modularity of this model facilitates the depiction of the interplay among state variables, focusing on delineating the operational state of DFIGs in wind farms. Additionally, it is centered on discerning the impact of VSG control parameters on SSO, aiming to elucidate the effects of the series compensation level and control parameters on SSO. Subsequently, a methodology for computing the parameter selection area based on the Guardian map is introduced, leading to the determination of the parameter selection of DFIGs. Simulations and HIL experiments demonstrate that the established state-space model precisely captures the time domain characteristics of the entire wind field while proving instrumental in addressing the challenge of quantitatively analyzing the parameter selection area. The area delineated in this study serves as a foundation for designing the parameters and effectively enhancing the stability of wind power systems. Moreover, the proposed strategy for calculating the selection area based on the Guardian map offers valuable insights for devising SSO suppression strategies in wind farms.

Author Contributions: Methodology, Y.W.; Formal analysis, Y.W.; Resources, W.J.; Writing—original draft, Y.W.; Writing—review & editing, Y.W.; Visualization, F.C. and R.W.; Project administration, R.W. All authors have read and agreed to the published version of the manuscript.

Funding: This research was funded by the National Natural Science Foundation of China under Grant 52307194, in part by the Young Elite Scientists Sponsorship Program by CAST under Grant YESS20230026, in part by the Guangdong Basic and Applied Basic Research Foundation under Grant 2021A1515110915, in part by the Fundamental Research Funds for the Central Universities in China under Grant N2204014, Liaoning Provincial Science and Technology Program-Natural Science Foundation of the Department of Science and Technology under Grant 2023-BS-056.

Data Availability Statement: Data are contained within the article.

Conflicts of Interest: The authors declare no conflicts of interest.

References

1. Wu, Y.; Zhang, P. Online Monitoring for Power Cables in DFIG-Based Wind Farms Using High-Frequency Resonance Analysis. *IEEE Trans. Sustain. Energ.* **2022**, *13*, 378–390. [[CrossRef](#)]
2. Jin, W.; Lu, Y. Stability analysis and oscillation mechanism of the DFIG-based wind power system. *IEEE Access* **2019**, *7*, 88937–88948. [[CrossRef](#)]
3. Almozayen, M.A.; Knight, A.M. Modeling the Impact of System Disturbances on Grid-Connected DFIG Using Dynamic Phasor FEM. *IEEE Trans. Ind. Appl.* **2024**, *60*, 132–143. [[CrossRef](#)]
4. Yu, Z.; Lin, J.; Liu, F.; Li, J.; Zhao, Y.; Song, Y.; Song, Y.; Zhang, X. Optimal Sizing and Pricing of Grid-Connected Renewable Power to Ammonia Systems Considering the Limited Flexibility of Ammonia Synthesis. *IEEE Trans. Power Syst* **2024**, *39*, 3631–3648. [[CrossRef](#)]
5. Abdelghany, M.B.; Al-Durra, A.; Gao, F. A Coordinated Optimal Operation of a Grid-Connected Wind-Solar Microgrid Incorporating Hybrid Energy Storage Management Systems. *IEEE Trans. Sustain. Energ.* **2024**, *15*, 39–51. [[CrossRef](#)]
6. Verma, P.K.S.; Dwivedi, B. A Cooperative Approach of Frequency Regulation Through Virtual Inertia Control and Enhancement of Low Voltage Ride-through in DFIG-based Wind Farm. *J. Mod. Power Syst. Clean Energy* **2022**, *10*, 1519–1530. [[CrossRef](#)]
7. Costa, N.E.; Revel, G.; Alonso, D.M.; Fernández, R.D. Detection of the stability boundary associated to subsynchronous oscillations in DFIG based wind farms. *Int. J. Electr. Power Energy Syst.* **2023**, *146*, 108783. [[CrossRef](#)]
8. Xu, J.; Lin, Y. Energy Management for Hybrid Electric Vehicles Using Safe Hybrid-Action Reinforcement Learning. *Mathematics* **2024**, *12*, 663. [[CrossRef](#)]
9. Shi, F.; Shu, D.; Yan, Z.; Song, Z. A shifted frequency impedance model of doubly fed induction generator (DFIG)-based wind farms and its applications on S2SI analysis. *IEEE Trans Power Electron* **2021**, *36*, 215–227. [[CrossRef](#)]
10. Han, J.; Feng, X.; Zhao, H.; Hu, P.; He, C. Adaptive VSG control strategy considering energy storage SOC constraints. *Front. Energy Res.* **2023**, *11*, 1278648. [[CrossRef](#)]
11. Gu, K.; Wu, F.; Zhang, X.P.; Ju, P.; Zhou, H.; Luo, J.; Li, J. SSR Analysis of DFIG-Based Wind Farm With VSM Control Strategy. *IEEE Access* **2019**, *7*, 118702–118711. [[CrossRef](#)]

12. Verma, P.; Seethalekshmi, K.; Dwivedi, B. A self-regulating virtual synchronous generator control of doubly fed induction generator-wind farms. *Can. J. Electr. Comput. Eng.* **2023**, *46*, 35–43. [\[CrossRef\]](#)
13. Liang, S.; Jin, S.; Shi, L. Research on control strategy of grid-connected brushless doubly-fed wind power system based on virtual synchronous generator control. *CES Trans. Electr. Mach. Syst.* **2022**, *6*, 404–412. [\[CrossRef\]](#)
14. Ouyang, J.; Tang, T.; Yao, J.; Li, M. Active voltage control for DFIG-based wind farm integrated power system by coordinating active and reactive powers under wind speed variations. *IEEE Trans. Energy Convers.* **2019**, *34*, 1504–1511. [\[CrossRef\]](#)
15. Mohanty, S.K.; Nayak, P.K.; Bera, P.K.; Alhelou, H.H. An Enhanced Protective Relaying Scheme for TCSC Compensated Line Connecting DFIG-Based Wind Farm. *IEEE Trans. Ind. Inform.* **2024**, *20*, 3425–3435. [\[CrossRef\]](#)
16. Sewdien, V.; Preece, R.; Torres, J.R.; van der Meijden, M. Systematic Procedure for Mitigating DFIG-SSR Using Phase Imbalance Compensation. *IEEE Trans. Sustain. Energ.* **2022**, *13*, 101–110. [\[CrossRef\]](#)
17. Puchalapalli, S.; Singh, B.; Das, S. Grid-Interactive Smooth Transition Control of Wind-Solar-DG Based Microgrid at Unpredictable Weather Conditions. *IEEE Trans. Ind. Appl.* **2024**, *60*, 1519–1529. [\[CrossRef\]](#)
18. Tao, H.; Hu, H.; Wang, X.; Blaabjerg, F.; He, Z. Impedance-based harmonic instability assessment in a multiple electric trains and traction network interaction system. *IEEE Trans. Ind. Appl.* **2018**, *54*, 5083–5096. [\[CrossRef\]](#)
19. Zou, X.; Du, X.; Tai, H.-M. Two-variable admittance model for D-PMSG-based wind turbine and stability criterion based on magnitude and phase contour plot. *IEEE Trans. Power Electron.* **2020**, *35*, 1484–1498. [\[CrossRef\]](#)
20. Zhang, C.; Cai, X.; Molinas, M. Frequency-domain modelling and stability analysis of a DFIG-based wind energy conversion system under non-compensated AC grids: Impedance modelling effects and consequences on stability. *IET Power Electron.* **2019**, *12*, 907–914. [\[CrossRef\]](#)
21. Sun, J.; Vieto, I. Development and application of type-III turbine impedance models including DC bus dynamics. *IEEE Open J. Power Electron.* **2020**, *1*, 513–528. [\[CrossRef\]](#)
22. Chi, Y.; Tang, B.; Hu, J.; Tian, X.; Tang, H.; Li, Y.; Sun, S.; Shi, L.; Shuai, L. Overview of mechanism and mitigation measures on multi-frequency oscillation caused by large-scale integration of wind power. *CSEE J. Power Energy Syst.* **2019**, *5*, 433–443.
23. Wang, H.; Buchhagen, C.; Sun, J. Methods to aggregate turbine and network impedance for wind farm resonance analysis. *IET Renew. Power Gener.* **2020**, *14*, 1304–1311. [\[CrossRef\]](#)
24. Zong, H.; Lyu, J.; Cai, X.; Rao, F.; Zhang, C.; Molinas, M. Modified single-machine aggregation of wind farms based on parameter identification of the impedance network. In Proceedings of the IEEE Power & Energy Society General Meeting (PESGM) 2019, Atlanta, GA, USA, 4–8 August 2019; pp. 1–5.
25. Rogers, G. *Power System Oscillations*; The Springer International Series in Engineering and Computer Science; Springer: Boston, MA, USA, 2000.
26. Wang, Y.; Wang, X.; Chen, Z.; Blaabjerg, F. Small-signal stability analysis of inverter-fed power systems using component connection method. *IEEE Trans. Smart Grid.* **2018**, *9*, 5301–5310. [\[CrossRef\]](#)
27. Krivulin, N.; Garg, A. Tropical Modeling of Battery Swapping and Charging Station. *Mathematics* **2024**, *12*, 644. [\[CrossRef\]](#)
28. Yang, D.; Wang, X. Unified modular state-space modeling of grid-connected voltage-source converters. *IEEE Trans. Power Electron.* **2020**, *35*, 9700–9715. [\[CrossRef\]](#)
29. Gu, Y.; Bottrell, N.; Green, T.C. Reduced-order models for representing converters in power system studies. *IEEE Trans. Power Electron.* **2018**, *33*, 3644–3654. [\[CrossRef\]](#)
30. Gong, H.; Yang, D.; Wang, X. Impact Analysis and Mitigation of Synchronization Dynamics for DQ Impedance Measurement. *IEEE Trans. Power Electron.* **2019**, *34*, 8797–8807. [\[CrossRef\]](#)
31. Song, J.X.; Gao, J.W.; Yu, H.S.; Liu, H.B. Quadratic stability of uncertain large-scale networked systems. *J. Control. Decis.* **2023**, *1*–9. [\[CrossRef\]](#)
32. Rui, W.; Qiuye, S.; Dazhong, M.; Xuguang, H. Line Impedance Cooperative Stability Region Identification Method for Grid-Tied Inverters Under Weak Grids. *IEEE Trans. Smart Grid.* **2020**, *11*, 2856–2866. [\[CrossRef\]](#)
33. Wang, R.; Sun, Q.; Hu, W.; Li, Y.; Ma, D.; Wang, P. SoC-Based Droop Coefficients Stability Region Analysis of the Battery for Stand-Alone Supply Systems With Constant Power Loads. *IEEE Trans. Power Electron.* **2021**, *36*, 7866–7879. [\[CrossRef\]](#)
34. Essallah, S.; Bouallegue, A.; Khedher, A. Integration of automatic voltage regulator and power system stabilizer: Small-signal stability in DFIG-based wind farms. *J. Mod. Power Syst. Clean Energy* **2019**, *7*, 1115–1128. [\[CrossRef\]](#)
35. Pan, Y.; Liu, F.; Chen, L.; Wang, J.; Qiu, F.; Shen, C.; Mei, S. Towards the Robust Small-Signal Stability Region of Power Systems Under Perturbations Such as Uncertain and Volatile Wind Generation. *IEEE Trans. Power Syst.* **2018**, *33*, 1790–1799. [\[CrossRef\]](#)

Disclaimer/Publisher’s Note: The statements, opinions and data contained in all publications are solely those of the individual author(s) and contributor(s) and not of MDPI and/or the editor(s). MDPI and/or the editor(s) disclaim responsibility for any injury to people or property resulting from any ideas, methods, instructions or products referred to in the content.